VARIATIONAL MULTI-SCALE MODELING FOR PARTICLE-LADEN GRAVITY CURRENTS OVER FLAT AND TRIANGULAR WAVY TERRAINS

BY

NING LIU

THESIS

Submitted in partial fulfillment of the requirements
for the degree of Master of Science in Civil Engineering
in the Graduate College of the
University of Illinois at Urbana-Champaign, 2019

Urbana, Illinois

Adviser:

Assistant Professor Jinhui Yan

Abstract

We deploy the residual-based variational multi-scale (RBVMS) method for simulating dilute particle-laden currents at large Reynolds number $Re = 10000$. The physical model is based on the coupling balance of fluid momentum and convection and diffusion. We derive the RBVMS formulation for the weak form of governing equations, design the fine scale parameters and make coupling between fluid momentum equations and density concentration equation. The proposed formulation is utilized to simulate the lock-exchange particle-laden gravity currents.

In this paper, two sets of simulations based on the finite element method are conducted on the Stampede2, TACC to validate the models. Firstly, we design a simple physical case that gravity currents over flat terrains in lock-exchange box. Two mesh with the different resolutions are constructed to observe convergence properties of the mesh resolution based on the RBVMS method. Flow statistics are compared against direct numerical simulations (DNS) results and experimental results in the literature and it shows that our computational models is able to simulate quite accurate results with even much lower mesh resolution. Then, the particle-laden gravity currents over triangular wavy terrains with changing wave height are further investigated. The effect of the wave height on the flow statistics is discussed.

From the good match between our simulation statistics and DNS or experimental data, it demonstrates that the model we build with RBVMS is able to capture physics of the particle-laden currents. The lower resolution mesh produces quite accurate results. The finite element formulation is stabilized by the RBVMS method in an unstructured mesh.

Keywords: Particle-laden flows, RBVMS, Lock-exchange gravity currents

To my lovely girlfriend, Niyu, and my friends.

To my Father and Mother.

Without your support and company I would not be here.

Acknowledgments

This project would not have been possible without the support of many people. Many thanks to my adviser, Dr.Jinhui Yan, who read my numerous revisions and helped make some sense of the confusion. Also thanks to Dr.Songzhe Xu, who offered guidance patience and support. He offered lots of nice and brilliant ideas and suggestion when I was a freshman in the CFD area. Finally, I would like to thank my colleagues Qiming Zhu for his help to complete this research, always offering support and help.

The results described in this thesis have been compiled into a journal paper and are under peer review. The citation is as follows: S. Xu, N. Liu, J. Yan*, Residual-based variational multi-scale modeling for particle-laden gravity currents over flat and triangular wavy terrains, submitted (2018).

Table of Contents

Chapter 1

Introduction

1.1 Background and Motivation

Many natural fluid dynamical processes involve complex particle-laden gravity currents. It refers to a class that consists with of two-phase fluid flow. One of phases is continuously connected which is also referred as the continuous carrier phase and the other one is small, immersible, and dilute particles which is also referred as dispersed or particle phase. And this current is driven by density differences. Examples of such flows in nature include thunderstorm fronts, volcano eruptions, oil spills in the ocean, snow avalanches, the release of contaminants in the environment, and flows generated by the collapse of a building [1, 2]. Numerical study of particle-laden gravity currents is important for understanding the associated environmental and geophysical physics. To model the dilute particle-laden gravity currents, the Eulerian-Eulerian approach which consists of the Navier-Stokes (NS) equations of incompressible flows and an advection-diffusion transport equation is typically used [3–15]. The coupling between them is through the Boussinesq approximation introduced in the fluid momentum equation to represent the gravitational effect associated with small density variations. However, in many cases, these particle-laden gravity currents are extremely high-Reynolds number turbulent flows, in which the carrier fluid violently exchanges mass, momentum, and energy with a dispersed particle field, rendering accurate numerical simulations of particle-laden gravity currents quite challenging and expensive.

1.2 Literature Review

Recently, there were several successful numerical efforts for the simulations for particle-laden gravity currents [16–18]. Hartel et al. [11, 12] utilized a spectral element method to investigate the 3D flow structure of lock-exchange configuration. Necker et al. [19] present 2D and 3D high-resolution simulations of particle-laden gravity currents also by spectral element method taking into account the sedimentation of the particles and the influence of particle settling on the flow dynamics. Elias et al. [20] developed a stabilized finite element formulation to simulate particle-laden gravity currents in both planar and cylindrical configurations. A variational multi-scale formulation for particle-laden gravity

currents is developed in Guerra et al. [21]. Numerical methods using adaptive meshes for particle-laden gravity currents can be found in Callaghan et al. [22], Hiester et al. [23], Koltakov and Fringer [24], and Rossa and Coutinho [25]. Aiming to accurately simulate high Reynolds number particle-laden gravity currents in complex geometry configurations with relative coarse mesh, a new residual-based variational multi-scale formulation (RBVMS), which represents the coupling between velocity field and density field in the fine-scale terms, is developed for particle-laden gravity currents in this paper. The original RBVMS was proposed in [26] for the simulation of incompressible turbulent flows. Since then, several research work in [27–38] have shown that RBVMS is able to produce accurate solutions on meshes with large-eddy simulation (LES)-level resolution that converge rapidly to the direct numerical simulation (DNS) results. The flexibility of RBVMS allows an easy extension to Arbitrary Lagrangian-Eulerian variational multiscale (ALE-VMS) framework [39–43], a moving domain formulation through the ALE [44] technique, which is widely used in the applications of high Reynolds number flows with moving boundaries and interfaces, such as offshore wind turbines and tidal turbines [45–47], compliant hydrofoils [48, 49], patient-specific cardiovascular mechanics [50–52], vehicle engineering [53], gas turbines [54], long-span bridges [55], and bioprosthetic heart valves [56, 57].

1.3 Objectives and Approach

The proposed formulation is utilized to simulate the particle-laden gravity currents in the lock-exchange configuration. In this setup, two fluids with different densities are initially at rest and confined in a container, separated by a barrier. After the barrier is removed, due to gravity, the heavier fluid invades the lighter fluid resulting in a density current. Many fundamental physics, such as the turbulent structures of the currents, settling or resuspension, and their effects on the particle transport, can be represented in this setup by controlled laboratory tests or numerical simulations [58], with high fidelity experimental and computational data available in the literature [19, 59]. In this paper, the particle-laden gravity currents in standard lock-exchange configuration with a flat terrain is simulated first as the validation for the proposed formulation. Then, the particle-laden gravity currents over triangular wavy terrains with changing wave height are simulated. The effect of the wave height on the flow statistics is investigated.

The governing equations of particle-laden gravity currents are presented in Chapter 2. The new RBVMS formulation is stated in Section 3. In Section 4.1, the particle-laden gravity currents in a lock-exchange configuration with a flat terrain is simulated at Re = 10,000. Comparison with direct numerical simulation (DNS) results and experimental results is presented in this section. In Section 4.2, the simulations of particle-laden gravity currents in a lock-exchange configuration with triangular wavy terrains are presented. The effect of wave height on flow physics is also discussed in this section. The conclusion is drawn in Chapter 5.

Chapter 2

Governing Equations of Particle-laden Gravity Currents at The Continuous Level

We start to build the physical model based on classic mechanics. In various situations of interest, the density difference in particle-laden gravity currents is less than 1%, making the Boussinesq approximation valid, in which the density is treated as constant in the momentum equation augmented with a body forcing term [3]. In this case, we can employ a Eulerian -Eulerian formulation, in which a continuum advection-diffusion equation is utilized to model the particle concentration field, instead of tracking individual particles in a Lagrangian fashion. In this paper, the particle diameter $\tilde{d}_p$ is assumed to be smaller than the Kolmogorov scale in turbulent flows, and the aerodynamic response time is assumed to be significantly smaller than the smallest time scale of the flow, making the particle Stokes number far less than 1.

Due to the small particle volume fraction of dilute gravity currents, we can assume that the fluid velocity is divergence free and the fluid-particle interaction is primarily through the exchange of momentum. The particles are transported by a velocity $\tilde{\boldsymbol{u}}_p$ that is obtained by superimposing the fluid velocity $\tilde{\boldsymbol{u}}$ and particle settling velocity $\tilde{u}_s \boldsymbol{e}_g$ in gravitational direction, and given as

$$\tilde{\boldsymbol{u}}_p = \tilde{\boldsymbol{u}} + \tilde{u}_s \boldsymbol{e}_g \tag{2.1}$$

where $\boldsymbol{e}_g$ is the unit vector in gravitational direction. $\tilde{u}_s$ is obtained by balancing the gravitational force with the Stokes drag force $\tilde{\boldsymbol{F}} = 3\pi\tilde{\mu}\tilde{d}_p(\tilde{\boldsymbol{u}} - \tilde{\boldsymbol{u}}_p)$, and given as

$$\tilde{u}_s = \frac{\tilde{d}_p^2(\rho_p - \rho_1)\tilde{g}}{18\tilde{\mu}} \tag{2.2}$$

where $\tilde{\mu}$ is the dynamic viscosity of the carrier fluid, $\tilde{g}$ is the gravitational acceleration magnitude, ρ_g is the density of the particle, and ρ_1 is the density of the carrier fluid. This equation is derived by the balance of vertical force including buoyancy, gravity and Stokes drag force. Note that the particle settling velocity is single-valued and the convective velocity for the particles is still divergence free.

With the above assumptions, the governing equations of dilute particle-laden gravity currents are stated as follows. The current motion is governed by the incompressible Navier-Stokes equations, which consists of a continuity equation

and momentum equations augmented by the force exerted on the fluid by the particles. In dimensional form, these equations read

$$\tilde{\rho}\left(\frac{\partial \tilde{\boldsymbol{u}}}{\partial \tilde{t}} + \tilde{\boldsymbol{u}} \cdot \boldsymbol{\nabla}\tilde{\boldsymbol{u}}\right) + \boldsymbol{\nabla}\tilde{p} - \tilde{\mu}\Delta\tilde{\boldsymbol{u}} - \tilde{\boldsymbol{f}}_p = \boldsymbol{0} \tag{2.3}$$

$$\boldsymbol{\nabla} \cdot \tilde{\boldsymbol{u}} = 0 \tag{2.4}$$

where $\tilde{\boldsymbol{u}}$ and $\tilde{p}$ are the current velocity and pressure, $\tilde{\rho}$ is the density of the gravity current, $\tilde{\mu}$ is the dynamic viscosity of the current. The additional forcing term in the momentum equation is given by $\tilde{\boldsymbol{f}}_p = \tilde{\rho}\tilde{g}\boldsymbol{e}_g$.

The evolution of the density field $\tilde{\rho}$ is governed by the following advection-diffusion equation.

$$\frac{\partial \tilde{\rho}}{\partial \tilde{t}} + \tilde{\boldsymbol{u}}_p \cdot \boldsymbol{\nabla}\tilde{\rho} - \tilde{\alpha}\Delta\tilde{\rho} = 0 \tag{2.5}$$

where $\tilde{\alpha}$ is the molecular diffusivity of the density field.

We can nondimensionalize Eq. 2.3, Eq. 2.4, and Eq. 2.5 by a reference length scale, such as the half-height $\tilde{H}/2$ of a lock-exchange flow domain, the carrier fluid density $\tilde{\rho}_1$, and the buoyancy velocity $\tilde{u}_b = \sqrt{\frac{\tilde{g}'\tilde{H}}{2}}$, where $\tilde{g}' = \tilde{g}\frac{\Delta\tilde{\rho}}{\tilde{\rho}_1}$ indicates the reduced gravitational acceleration vector. Provided the above scales, the non-dimensional time, fluid velocity, particle convective velocity, pressure and density can be given by

$$t = \frac{2\tilde{t}\tilde{u}_b}{\tilde{H}}, \quad \boldsymbol{u} = \frac{\tilde{\boldsymbol{u}}}{\tilde{u}_b}, \quad \boldsymbol{u}_p = \frac{\tilde{\boldsymbol{u}}_p}{\tilde{u}_b}, \quad p = \frac{\tilde{p}}{\tilde{\rho}_1\tilde{u}_b^2}, \quad \rho = \frac{\tilde{\rho} - \tilde{\rho}_l}{\Delta\tilde{\rho}} \tag{2.6}$$

In the above equations, $\Delta\tilde{\rho} = \tilde{\rho}_h - \tilde{\rho}_l$ denotes the difference between the reservoir densities of heavy ($\tilde{\rho}_h$) and light fluid ($\tilde{\rho}_l$), respectively. After non-dimensionalization, we obtain

$$\frac{\partial \boldsymbol{u}}{\partial t} + \boldsymbol{u} \cdot \boldsymbol{\nabla}\boldsymbol{u} + \boldsymbol{\nabla}p - \frac{1}{Re}\Delta\boldsymbol{u} - \boldsymbol{f}_p = \boldsymbol{0} \tag{2.7}$$

$$\boldsymbol{\nabla} \cdot \boldsymbol{u} = 0, \tag{2.8}$$

$$\frac{\partial \rho}{\partial t} + \boldsymbol{u}_p \cdot \boldsymbol{\nabla}\rho - \frac{1}{ReS_c}\Delta\rho = 0 \tag{2.9}$$

where $\boldsymbol{f}_p = \rho\boldsymbol{e}_g$. The two dimensionless Reynolds number Re and Schmidt number S_c are defined as

$$Re = \frac{\tilde{\rho}_1\tilde{u}_b\tilde{H}}{2\tilde{\mu}} \tag{2.10}$$

$$S_c = \frac{\tilde{\mu}}{\tilde{\rho}_1\tilde{\alpha}} \tag{2.11}$$

The above equations, together with the appropriate initial and boundary conditions, constitute a complete mathe-

matical model of particle-laden gravity currents at the continuous level.

Chapter 3

Numerical Formulation of Particle-laden Gravity Currents

In order to obtain the stable numerical solutions of simulation, we begin with deriving the form of the governing equations based on finite element method and adopt the RBVMS to solve the coupled NavierStokes and density concentration equations stably. In the weak form formulation, we design different testing functions for velocity, pressure and density which are our objective values, multiply them on both sides of governing equations and conduct integration by parts. Then, when RBVMS is deployed in the weak form formulation, we try to build numerical model to represent to residual between simulation and exact solution and separate solution into two parts: fine solution and coarse solution. The coarse solution which depended on mesh solution is able to be solved accurately and we throw the rest part of solution which is lower than the current resolution of mesh into the fine scale solution. And it is easily and instinctively to assume the fine scale solution have a critical relationship with residual discussed above.

3.1 Weak Form Formulation

Let $\mathcal{V}$ denote the trial function space for the velocity, pressure, and density unknowns $\{\boldsymbol{u}, p, \rho\}$, and let $\mathcal{W}$ denote the test function space for the linear momentum, continuity, density equations $\{\mathbf{w}, q, \eta\}$. The weak form of the particle-laden gravity currents equations is stated as follows: find $\{\boldsymbol{u}, p, \rho\} \in \mathcal{V}$, such that $\forall \{\boldsymbol{w}, q, \eta\} \in \mathcal{W}$,

$$\boldsymbol{B}\left(\{\boldsymbol{w}, q, \eta\}, \{\boldsymbol{u}, p, \rho\}\right) = \boldsymbol{F}\left(\{\boldsymbol{w}, q, \eta\}\right) \tag{3.1}$$

where $\boldsymbol{B}$ and $\boldsymbol{F}$ are given as

$$\boldsymbol{B}\left(\{\boldsymbol{w}, q, \eta\}, \{\boldsymbol{u}, p, \rho\}\right) = \left(\boldsymbol{w}, \frac{\partial \boldsymbol{u}}{\partial t} + \boldsymbol{u} \cdot \boldsymbol{\nabla}\boldsymbol{u}\right)_{\Omega} + \left(\boldsymbol{\nabla}\boldsymbol{w}, -p\mathbf{I} + \frac{2}{Re}\boldsymbol{\nabla}^{S}\boldsymbol{u}\right)_{\Omega} + (q, \boldsymbol{\nabla}\cdot\boldsymbol{u})_{\Omega}$$
$$+ \left(\eta, \frac{\partial \rho}{\partial t} + \boldsymbol{u}_{p} \cdot \boldsymbol{\nabla}\rho\right)_{\Omega} + \left(\boldsymbol{\nabla}\eta, \frac{1}{ReS_{c}} \cdot \boldsymbol{\nabla}\rho\right)_{\Omega} \tag{3.2}$$

$$\boldsymbol{F}\left(\{\boldsymbol{w}, q, \eta\}\right) = \left(\boldsymbol{w}, \boldsymbol{f}_{p}\right)_{\Omega} + (\boldsymbol{w}, \boldsymbol{h})_{\Gamma_{h}} + (\eta, h)_{\Gamma_{h_{p}}} \tag{3.3}$$

where $\boldsymbol{\nabla}^{S}$ is the symmetric gradient operator, $\boldsymbol{h}$ is the applied traction and h is the applied density flux.

3.2 RBVMS Application in The Formulation

The residual-based variational multi-scale formulation (RBVMS) is adopted to numerically solve the coupled Navier–Stokes and density concentration equations. In RBVMS, the trial function space and test function space are orthogonally decomposed into two parts, namely, $\mathcal{V} = \mathcal{V}^{h} \oplus \mathcal{V}'$ and $\mathcal{W} = \mathcal{W}^{h} \oplus \mathcal{W}'$, where the variables with superscript h denote the coarse-scale velocity, pressure, and density fields, which are resolved by the given problem mesh, and the variables with superscript $'$ denote the unresolved or fine-scale components, the effects of which on the solutions need to be modeled. With the above decomposition, the solution fields split into two parts, namely,

$$\boldsymbol{u} = \boldsymbol{u}^{h} + \boldsymbol{u}' \tag{3.4}$$

$$p = p^{h} + p' \tag{3.5}$$

$$\rho = \rho^{h} + \rho' \tag{3.6}$$

Substituting the above decomposition into the weak form given by Eq. 3.1, and restricting the test functions to reside in the space of coarse-scales, gives the following semi-discrete RBVMS formulation: Find $\{\boldsymbol{u}^{h}, p^{h}, \rho^{h}\} \in \mathcal{V}^{h}$, such that $\forall \{\mathbf{w}^{h}, q^{h}, \eta^{h}\} \in \mathcal{W}^{h}$,

$$\boldsymbol{B}_{RBVMS}\left(\{\boldsymbol{w}^{h}, q^{h}, \eta^{h}\}, \{\boldsymbol{u}^{h}, p^{h}, \rho^{h}\}\right) = \boldsymbol{F}_{RBVMS}\left(\{\boldsymbol{w}^{h}, q^{h}, \eta^{h}\}\right) \tag{3.7}$$

where $\boldsymbol{B}_{RBVMS}\left(\{\boldsymbol{w}^h, q^h, \eta^h\}, \{\boldsymbol{u}^h, p^h, \rho^h\}\right)$ and $\boldsymbol{F}_{RBVMS}\left(\{\boldsymbol{w}^h, q^h, \eta^h\}\right)$ are given as

$$\begin{aligned}
&\boldsymbol{B}_{RBVMS}\left(\{\boldsymbol{w}^h, q^h, \eta^h\}, \{\boldsymbol{u}^h, p^h, \rho^h\}\right) = \boldsymbol{B}\left(\{\boldsymbol{w}^h, q^h, \eta^h\}, \{\boldsymbol{u}^h, p^h, \rho^h\}\right) \\
&- \sum_{e=1}^{nel}\left(\boldsymbol{u}^h \cdot \boldsymbol{\nabla}\boldsymbol{w}^h + \boldsymbol{\nabla} q^h, \boldsymbol{u}'\right)_{\Omega^e} - \sum_{e=1}^{nel}\left(\boldsymbol{\nabla}\cdot\boldsymbol{w}^h, p'\right)_{\Omega^e} + \sum_{e=1}^{nel}\left(\boldsymbol{w}^h, \boldsymbol{u}'\cdot\boldsymbol{\nabla}\boldsymbol{u}^h\right)_{\Omega^e} \\
&- \sum_{e=1}^{nel}\left(\boldsymbol{\nabla}\boldsymbol{w}^h, \boldsymbol{u}'\otimes\boldsymbol{u}'\right)_{\Omega^e} - \sum_{e=1}^{nel}\left(\boldsymbol{u}^h, \boldsymbol{\nabla}\eta^h\rho'\right)_{\Omega^e}
\end{aligned} \tag{3.8}$$

$$\boldsymbol{F}_{RBVMS}\left(\{\boldsymbol{w}^h, q^h, \eta^h\}\right) = \boldsymbol{F}\left(\{\boldsymbol{w}^h, q^h, \eta^h\}\right) \tag{3.9}$$

In the above equation, the fine-scale velocity, pressure, and density fields are modeled to be proportional to the residuals of the strong form momentum, continuity, and density concentration equations, given by

$$\begin{Bmatrix} \boldsymbol{u}' \\ \rho' \end{Bmatrix} = -\left\{\boldsymbol{\tau}\right\}\begin{Bmatrix} \boldsymbol{r}_m(\boldsymbol{u}^h, p^h, \rho^h) \\ r_\rho(\boldsymbol{u}^h, \rho^h) \end{Bmatrix} \tag{3.10}$$

$$p' = -\tau_c r_c(\boldsymbol{u}^h) \tag{3.11}$$

where $\boldsymbol{\tau}$ and τ_c are the fine-scale parameters, which will be given in the following section. $\boldsymbol{r}_m(\boldsymbol{u}^h, p^h, \rho^h)$, $r_c(\boldsymbol{u}^h)$ and $r_\rho(\boldsymbol{u}^h, \rho^h)$ are the residuals of momentum equations, continuity equation, and density concentration equation, given as:

$$\boldsymbol{r}_m(\boldsymbol{u}^h, p^h, \rho^h) = \frac{\partial \boldsymbol{u}^h}{\partial t} + \boldsymbol{u}^h\cdot\boldsymbol{\nabla}\boldsymbol{u}^h + \boldsymbol{\nabla}p^h - \frac{1}{Re}\Delta\boldsymbol{u}^h - \rho^h\boldsymbol{e}_g \tag{3.12}$$

$$r_c(\boldsymbol{u}^h) = \boldsymbol{\nabla}\cdot\boldsymbol{u}^h \tag{3.13}$$

$$r_\rho(\boldsymbol{u}^h, \rho^h) = \frac{\partial \rho^h}{\partial t} + \boldsymbol{u}_p^h\cdot\boldsymbol{\nabla}\rho^h - \frac{1}{ReS_c}\Delta\rho^h \tag{3.14}$$

3.3 Definition of The Fine-scale Parameters

Following the developments of stabilized methods for advective–diffusive systems and compressible flows presented in [60–62] and the development of VMS for stratified turbulent flows in [36] , we assume the fine-scale parameters $\boldsymbol{\tau}$ is no longer a diagonal matrix, which is typically utilized by standard RBMVS approach for turbulent flows [26], and design $\overline{\boldsymbol{\tau}}$ as

$$\left\{\overline{\boldsymbol{\tau}}\right\} = \boldsymbol{B}^{-\frac{1}{2}} \tag{3.15}$$

where $\boldsymbol{B}$ is given by

$$\boldsymbol{B} = \boldsymbol{A}_0^2 + \boldsymbol{A}_i G_{ij} \boldsymbol{A}_j + C_I \boldsymbol{K}^2 G_{ij} G_{ij} \tag{3.16}$$

with the individual submatrices, $\boldsymbol{A}_0$, $\boldsymbol{A}_i$ and $\boldsymbol{K}$ defined as follows

$$\boldsymbol{A}_0 = \begin{Bmatrix} \frac{2}{\Delta t} & 0 & 0 & 0 \\ 0 & \frac{2}{\Delta t} & 0 & 0 \\ 0 & 0 & \frac{2}{\Delta t} & 1 \\ 0 & 0 & 0 & \frac{2}{\Delta t} \end{Bmatrix} \tag{3.17}$$

$$\boldsymbol{A}_i = \begin{Bmatrix} u_i \boldsymbol{I}_{3\times 3} & 0 \\ 0 & u_i + u_s \delta_{i3} \end{Bmatrix} \tag{3.18}$$

$$\boldsymbol{K} = \begin{Bmatrix} \frac{1}{Re} \boldsymbol{I}_{3\times 3} & 0 \\ 0 & \frac{1}{ReS_c} \end{Bmatrix}. \tag{3.19}$$

where Δt is the time step, C_I is a positive constant that is derived from an appropriate element-wise inverse [63], $\boldsymbol{I}_{3\times 3}$ is the identity matrix, and G_{ij} is the element mesh metric tensor, given by $G_{ij} = \frac{\partial \xi_i}{\partial x_k} \frac{\partial \xi_j}{\partial x_k}$, where $\frac{\partial \xi_j}{\partial x_k}$ is Jacobian matrix of the mapping between the parametric element and its corresponding physical element.

Substitute $\boldsymbol{A}_0$, $\boldsymbol{A}_i$ and $\boldsymbol{K}$ into Eq. 3.16 and take the square-root-inverse analytically, the stabilization matrix $\boldsymbol{\tau}$ are computed as

$$\boldsymbol{\tau} = \begin{Bmatrix} \tau_m & 0 & 0 & 0 \\ 0 & \tau_m & 0 & 0 \\ 0 & 0 & \tau_m & \overline{\tau}_{u\rho} \\ 0 & 0 & 0 & \tau_\rho \end{Bmatrix} \tag{3.20}$$

where τ_m and τ_c are

$$\tau_m = \left(\frac{4}{\Delta t^2} + u_i^h G_{ij} u_j^h + \frac{C_I}{Re^2} G_{ij} G_{ij} \right)^{-1/2}, \tag{3.21}$$

$$\tau_\rho = \left(\frac{4}{\Delta t^2} + (u_i^h + u_s^h \delta_{i3}) G_{ij} (u_j^h + u_s^h \delta_{j3}) + \frac{C_I}{Re^2 S_c^2} G_{ij} G_{ij} \right)^{-1/2} \tag{3.22}$$

In the above stabilization matrix construction process, it turns out that τ_m and τ_ρ are the standard scalar-valued parameters employed in the stabilized variational multi-scale formulations of incompressible flows and advection-diffusion equations [39–41, 64–69]. The off-diagonal term $\overline{\tau}_{u\rho}$, representing the coupling between velocity field and density concentration field, is given as

$$\overline{\tau}_{u\rho} = -\frac{4}{\Delta t(\tau_m^{-1}\tau_\rho^{-2} + \tau_m^{-2}\tau_\rho^{-1})} \tag{3.23}$$

In this work, we assume the fine-scale parameter of pressure remains the usual definition, namely,

$$\tau_c = \frac{1}{G_{ii}\tau_M} \tag{3.24}$$

Note that summation is taken on the repeated indices in the above equations

Chapter 4

Numerical Simulations of Particle-laden Currents

In this chapter, we design two cases of simulation based on one of the most popular configuration of experiments and DNS examples so that it is persuadable and convenient to compare results with reference data. Gmsh is utilized to build frame mesh with two different resolutions and all the work is based on the Fortran code. The size of configuration and parameters are described as following sections.

4.1 Lock-exchange Particle-laden Gravity Currents Over Flat Terrain

The problem of the lock-exchange gravity currents over a flat terrain is solved by the proposed formulation in this section. This problem is one of the most popular configurations for conducting laboratory experiments and high-resolution simulations on particle-laden gravity currents, which is an excellent example for validation purpose. The computational domain is a rectangular box with dimension $L_x \times L_y \times L_z$, where uniformly suspended particle sediments are initially enclosed in a small portion of the domain with dimension $L_x^s \times L_y^s \times L_z^s$ separated by a barrier with clear fluid. The computational setup is shown in Fig. 4.1. Due to gravity, a mutual inverse interaction between the "heavy" particle-mixture flow and "light" clear fluid will happen. Such a problem was investigated experimentally in [70] and computationally using DNS in [59] and high-resolution simulation in [19]

4.1.1 Parameters of The Flat-terrain Case and Boundary Conditions

The simulation is performed using linear finite element discretization using unstructured tetrahedral elements with a uniform element length. Two element lengths of 0.066 and 0.033 are employed, which are denoted by "coarse mesh" and "fine mesh" next. A snapshot of the fine mesh close to the inlet is shown in Fig. 4.2. The statistics of the mesh are listed in Table 4.1. The time step $\Delta t = 2 \times 10^{-3}$ is employed for coarse mesh and $\Delta t = 1 \times 10^{-3}$ is employed for the fine mesh. The settling velocity is set to $u_s = 0.02$, corresponding to a middle silt, the Schmidt number $S_c = 1$, the Reynolds number $Re = 10,000$, which is the highest in the current literature.

The boundary conditions are given as follows. For fluid field, free-slip boundary conditions are imposed for the velocity field in the streamwise and spanwise directions while no-slip boundary conditions are used in the vertical di-

Table 4.1: Mesh statistics

Meshes	Element lenght	Total number of nodes	Total number of elements
Coarse	0.066	447,392	2,537,166
Fine	0.033	3,485,389	20,150,859

rection. For the scalar field, no-flux conditions are used in the streamwise and spanwise directions. At the top surface, a no-flux boundary condition is adopted at the top boundary as well. To take the settling velocity into consideration, this is achieved by imposing

$$u_s\rho - \frac{1}{S_c Re}\boldsymbol{\nabla}\rho \cdot \boldsymbol{n} = 0. \tag{4.1}$$

At the bottom surface, no erosion and re-suspension is allowed. In order to micmic the particles deposition process, an outflow boundary condition is used at the bottom surface, namely,

$$u_s\boldsymbol{\nabla}\rho \cdot \boldsymbol{n} + \frac{\partial\rho}{\partial t} = 0, \tag{4.2}$$

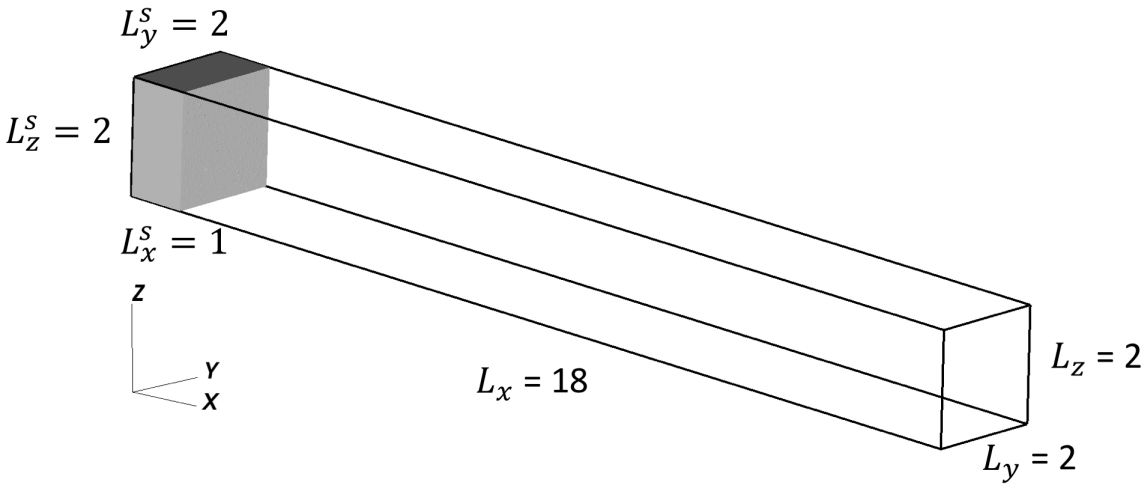

Figure 4.1: Computational setup of lock-exchange particle-laden gravity currents over flat terrain.

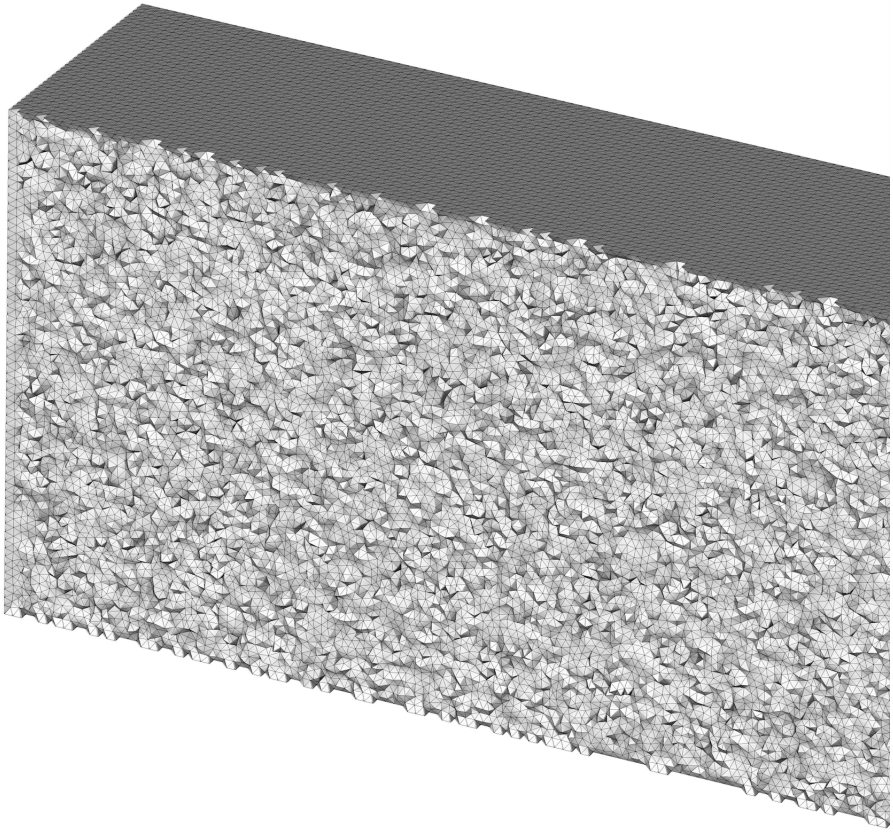

Figure 4.2: Mesh around the inlet of the fine mesh.

4.1.2 Discussion

The gravity-laden gravity current over flat terrain with the same parameters was also studied by DNS in [59] and high-resolution simulation in [19], where the element length is 8.45 times and 5.28 times finer, respectively, than the element length of the "coarse mesh" used in the present work. For more details of the grid utilized in these two computations, the readers are referred to the original papers in [59] and [19]. To validate the method, the results using the proposed formulation are thoroughly compared with these two computational results in [19, 59], and experimental results in [70] for the flow statistics where such data is available. In this section, three sets of data are compared with literature data discussed which are the time history of the front location of the particle-laden gravity current, the normalized suspended mass and sedimentation rate. These three sets of solution are significant characteristics of particle laden problems and are able to represents principle physical process.

Fig. 4.3 shows the time history of the front location $x^*(t)$ of the particle-laden gravity current. Good agreement is achieved between present results and the results from the DNS in [59] and the high-resolution simulation in [19]. The current front travels at a constant speed in the earlier stage, but experiences a significant deceleration at later times due to particles settling. The settling of particles also causes a continued loss of suspended material in the channel. Fig. 4.4 shows the time history of the suspended mass normalized by the initial suspended mass $\frac{m_p(t)}{m_p(0)}$, where $m_p(t)$ is defined as

$$\dot{m}_p(t) = \int_\Omega \rho d\Omega \tag{4.3}$$

Again, reasonable agreement with the two higher resolution simulations is achieved for both "coarse mesh" and "fine mesh". Rapid sedimentation process is observed in this plot. After $t = 21$, nearly 70 percent of all particles have settled out. Consequently, a sediment layer is formed at the bottom of the domain as time evolves. Fig. 4.5 shows the time history of the sedimentation rate $\dot{m}_s(t)$, which is defined as the time derivative of the total mass of sedimented particles per unit span

$$\dot{m}_s(t) = \frac{1}{L_y} \int_0^{L_x} \int_0^{L_y} \rho_w(x, y, t) u_s dx dy \tag{4.4}$$

where ρ_w is the density concentration at the bottom wall. Agreement is achieved for "coarse mesh" and "fine mesh". Until t =14, the sedimentation rate steadily increases, which indicates that the suspension stretches out along the bottom and remains almost undiluted. In this stage, the increase is roughly proportional to $t^{0.5}$ in the logarithmic representation. However, after t =14, a dramatical decay of sedimentation rate with time is observed, which is roughly

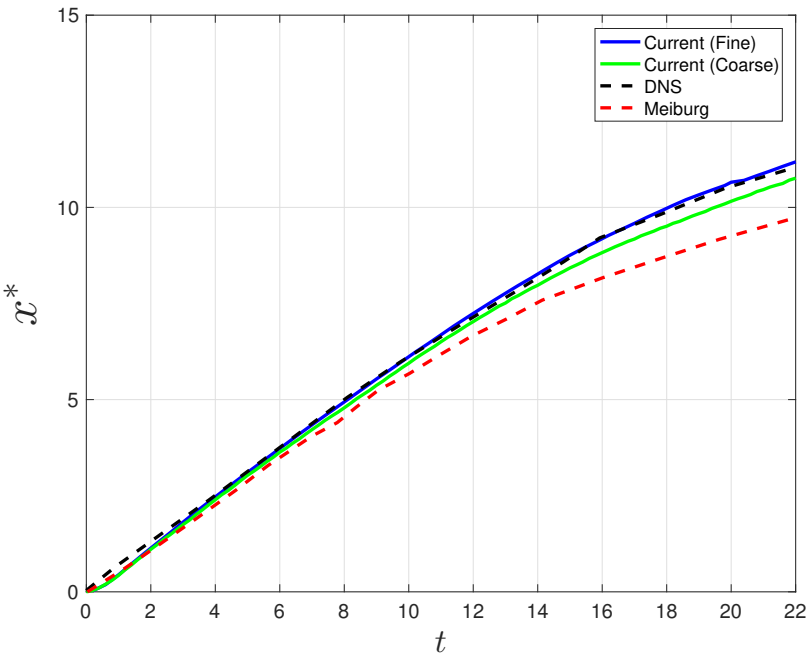

Figure 4.3: Time history of front location. The high-resolution simulation results in [19] and DNS results in [59] are also plotted for comparison.

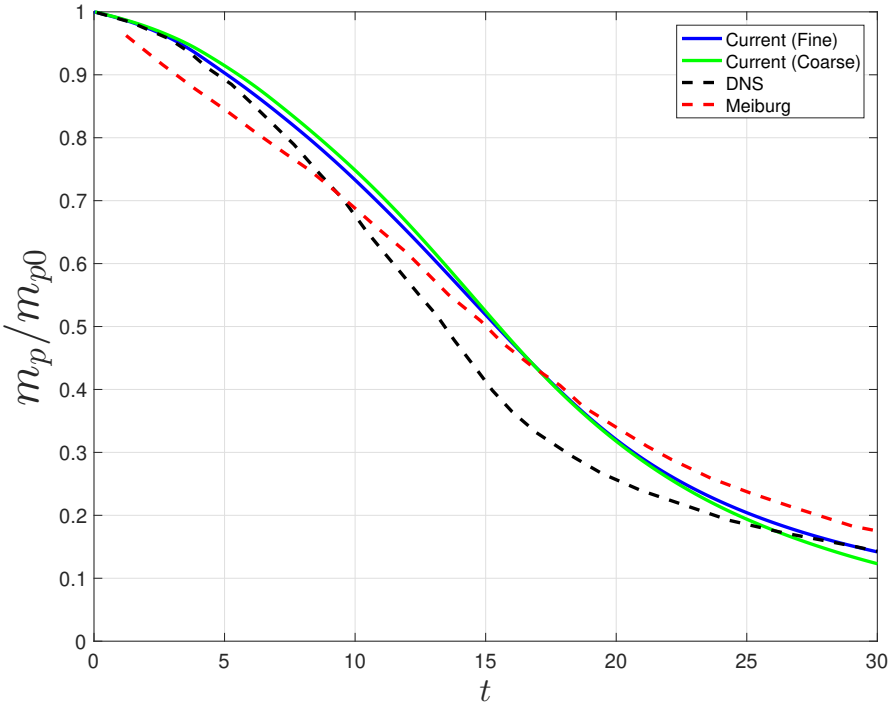

Figure 4.4: Time history of the normalized suspended mass. The high-resolution simulation results in [19] and DNS results in [59] are also plotted for comparison.

proportional to $t^{-2.36}$ in the logarithmic representation. This change occurs when about half the particles have settled out, and it also coincides with the time when the front speed of the current starts to decrease (see Fig. 4.3).

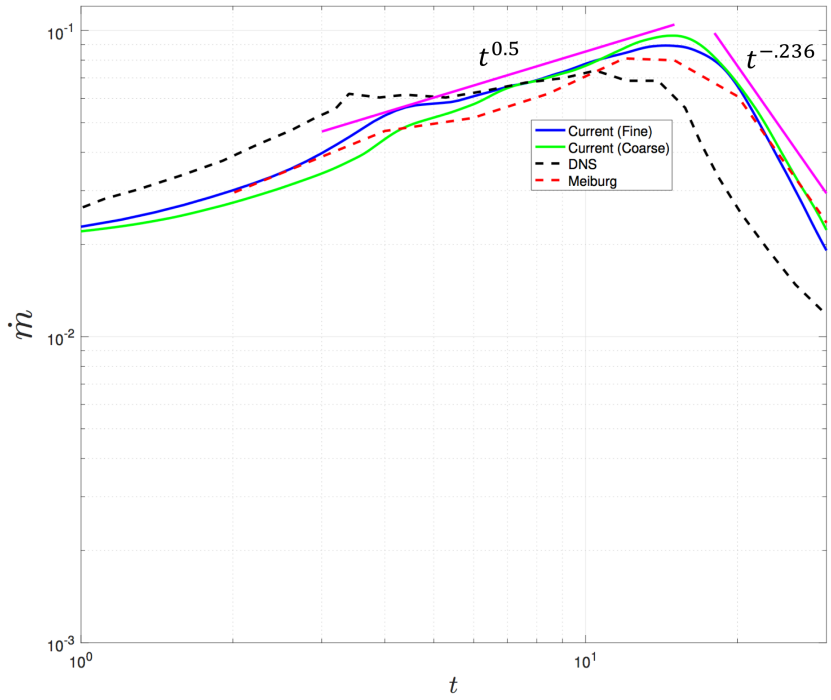

Figure 4.5: Time history of sedimentation rate. The high-resolution simulation results in [19] and DNS results in [59] are also plotted for comparison.

Another important quantity of the sedimentation process is the stream-wise deposit of the sediment particles, which can be quantified as

$$D_t(x,t) = \frac{1}{L_z^s L_x^s} \int_0^t \rho_w(x,t) u_s d\tau \tag{4.5}$$

The profile of $D_t(x, t = 7.3)$ and $D_t(x, t = 11)$ are plotted in Fig. 4.6. For $Re = 10{,}000$ and $u_s = 0.02$, experimental measurements are available in [70] and also plotted in Fig. 4.6 along with the DNS results. Good agreement with the experimental data and DNS results is seen for the both "coarse mesh" and "fine mesh". But clearly, the results based on fine mesh is much closer to DNS result.

In particle-laden gravity currents, the energy is converted from potential energy into fluid motion. The potential energy available is given by the elevation of the center of mass of the denser fluid relative to the light fluid. After the flow is initiated, kinetic energy is increased and potential energy is decreased. For the cases without replenishment of potential energy by a source, the fluid motion will ultimately decay due to viscous dissipation. In particle-laden gravity currents, energy dissipation is caused by both the gradients of convection and the Stokes flow around individual

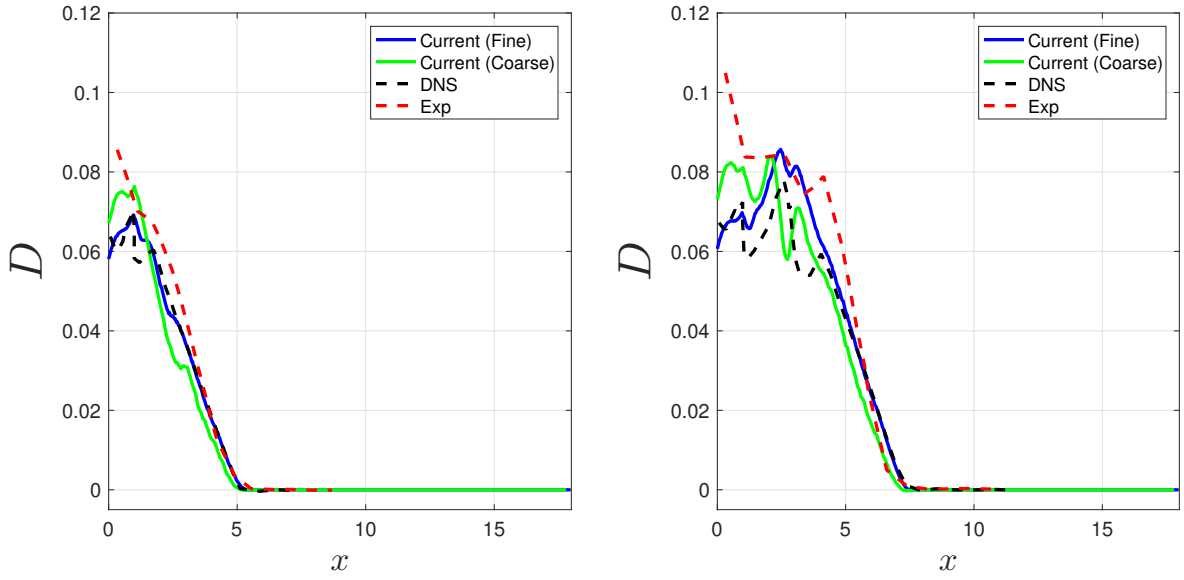

Figure 4.6: Particle deposit $D(x,t)$ along stream-wise direction at $t = 7.3$ (left) and 11 (right). The experimental data in [70] and DNS results in [59] are also plotted for comparison.

particles. The latter dissipation is equivalent to the potential energy loss that particles experience due to progressive settling, which can be computed by the product of the local concentration and the settling speed u_s.

For a time instant, the total potential energy $E_p(t)$, kinetic energy $k(t)$, and dissipated energy $E_v(t)$ and $E_s(t)$ are given as follows.

$$k(t) = \int_\Omega \frac{1}{2}\boldsymbol{u}\cdot\boldsymbol{u}d\Omega \tag{4.6}$$

$$E_p(t) = \int_\Omega \rho z d\Omega \tag{4.7}$$

$$E_v(t) = \int_0^t \left(\int_\Omega \frac{2}{Re}\boldsymbol{S}:\boldsymbol{S}d\Omega\right)d\tau \tag{4.8}$$

$$E_s(t) = \int_0^t \left(\int_\Omega u_s\rho d\Omega\right)d\tau \tag{4.9}$$

where $\boldsymbol{S} = \frac{1}{2}\left(\boldsymbol{\nabla u} + \boldsymbol{\nabla}^T\boldsymbol{u}\right)$ is the symmetric part of the velocity gradient. The time history of the above four terms are plotted in Fig. 4.7. Good agreement is obtained for $k(t)$, $E_p(t)$ and $E_s(t)$, while the dissipation due to the gradients of the (macroscopic) convective motion is underestimated, due to much lower resolution used in the present work.

Isosurfaces of constant particle concentration ($\rho = 0.25$) colored by velocity magnitude at five time instances are shown in Fig. 4.8. The DNS results from [59] are also shown for comparison. Both the coarse and fine mesh generate quite similar density profile as the DNS does. At time t = 8, when the current is fully developed, the typical 3D

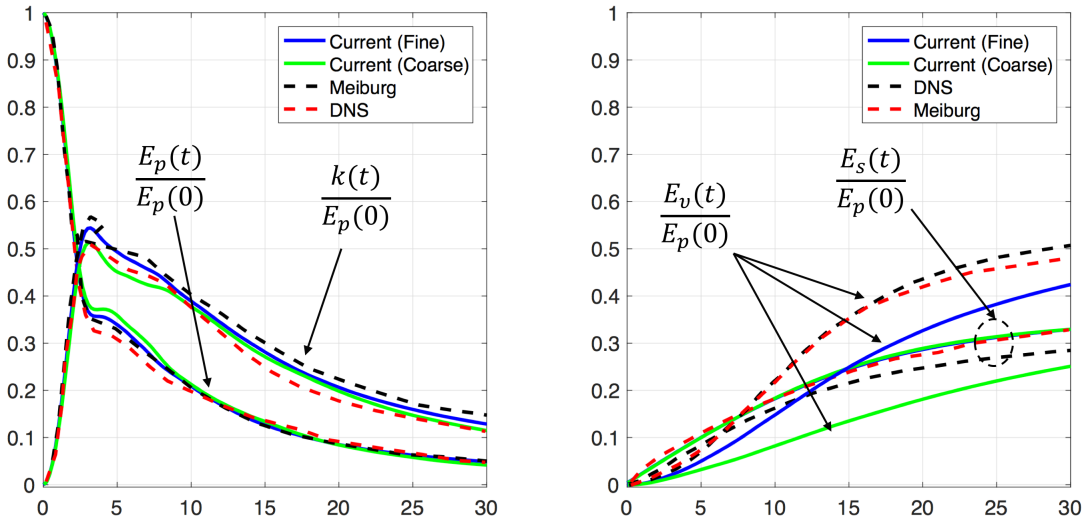

Figure 4.7: Time history of kinetic energy $k(t)$, potential energy $E_p(t)$, the energy dissipations $E_v(t)$ and $E_s(t)$ normalized by the initial potential energy $E_p(0)$. The experimental data in [19] and DNS results in [59] are also plotted for comparison.

lobe-and-cleft structure is observed in its front, as depicted in Fig. 4.9. It can been seen that as the time evolves, the currents develops a high 3D turbulence with strong stream wise vortices. This can be also supported by the complex vorticity structure visualized in Fig 4.10, where the Q-criterion is adopted and defined as

$$Q = \frac{1}{2}(\|\boldsymbol{\Omega}\|^2 - \|\boldsymbol{S}\|^2) \tag{4.10}$$

where $\boldsymbol{\Omega} = \frac{1}{2}\left(\boldsymbol{\nabla u} - \boldsymbol{\nabla}^T \boldsymbol{u}\right)$ is the anti-symmetric part of the velocity gradient. In Fig 4.10, we can see that the results from the coarse mesh lose some flow features of vorticity structure due to lower mesh resolution, while the fine mesh also produces quite similar vorticity structure like the DNS does.

4.2 Lock-exchange Particle-laden Gravity Currents Over Triangular Wavy Terrain

In this section, the particle-laden gravity currents over triangular wavy terrain are simulated. The effect of the height of the triangular waves on the flow physics is investigated. Fig. 4.11 shows the computational domain, which consists with a rectangular section with the same dimensions as used in the previous section, where uniformly suspended particle sediments are initially enclosed in, and a section with a triangular wavy bottom surface, with a length of 17. The length of the triangular waves is fixed to $S = 2$. Three different heights, $h = 0.05$, 0.1 and 0.2, are studied

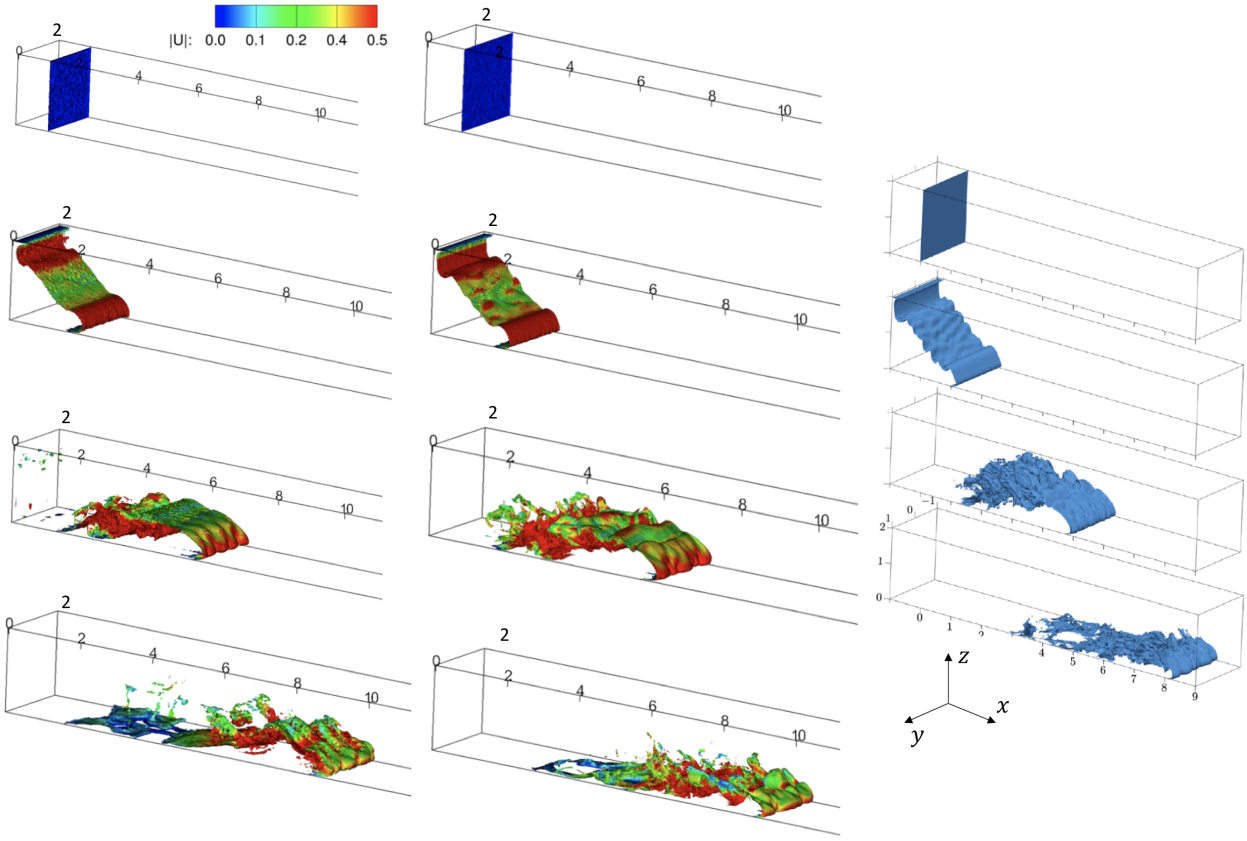

Figure 4.8: Interface evolution of $\rho = 0.25$ ($t = 0$, 2, 8 and 14, from top to bottom; coarse mesh, fine mesh, and DNS results from [59], from left to right).

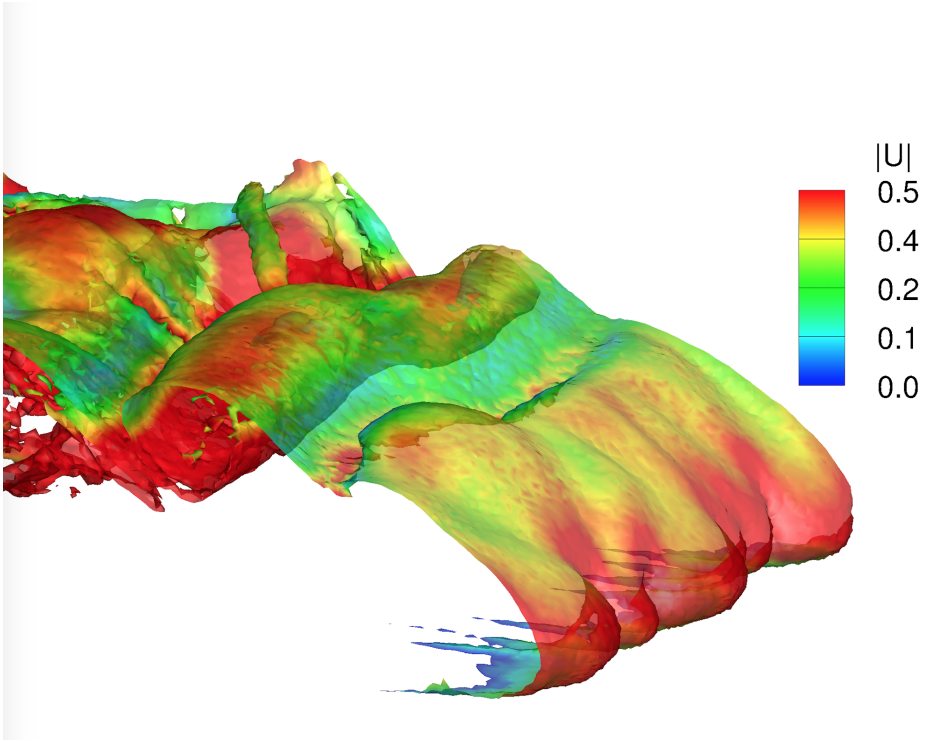

Figure 4.9: Zoom-in of the nose region of the current front in a concentration $\rho = 0.25$ at $t = 8$.

in this paper. Please note the case of $h = 0$ corresponds to flat terrain case simulated in the previous section. In order to show a direct comparison with the flat terrain case, the same Reynolds number, Schmidt number, settling velocity, boundary conditions are employed. The element length and time step based on the coarse mesh in the previous section are used again.

The iso-surface of density concentration $\rho = 0.25$ of the three cases with triangular wavy terrain at $t = 8$ and 14 is visualized in Fig. 4.16. Fig. 4.12 shows the time history of the front location. As the wave height increases, the speed of the front head gradually becomes slower. We also found that time, when the front speed starts to decrease, arrives earlier as the wave height increases. The normalized suspended mass is shown in Fig. 4.14. Settling processes becomes slower, as the wave height increases, which indicates that the triangular wavy bottom geometry not only decreases the front speed but also decreases the settling of particles. Fig. 4.13 shows the time history of sedimentation rate. When the wave height is not very high ($h = 0.05$ and 0.1), the sedimentation pattern is still quite similar to the flat terrain case, but for the case of $h = 0.2$, the sedimentation rate is noticeably changed. The power law of the increasing stage and delay stage of sedimentation rate no longer holds for this higher wave height case.

The time history of the normalized potential energy, kinetic energy, and energy dissipation are plotted in Fig. 4.15. For the cases of $h = 0.05$ and 0.1, the energy budget remains quite similar to the flat terrain case. But for $h = 0.2$, compared with other cases, we note the conversion of potential energy into kinetic energy becomes lower, while the

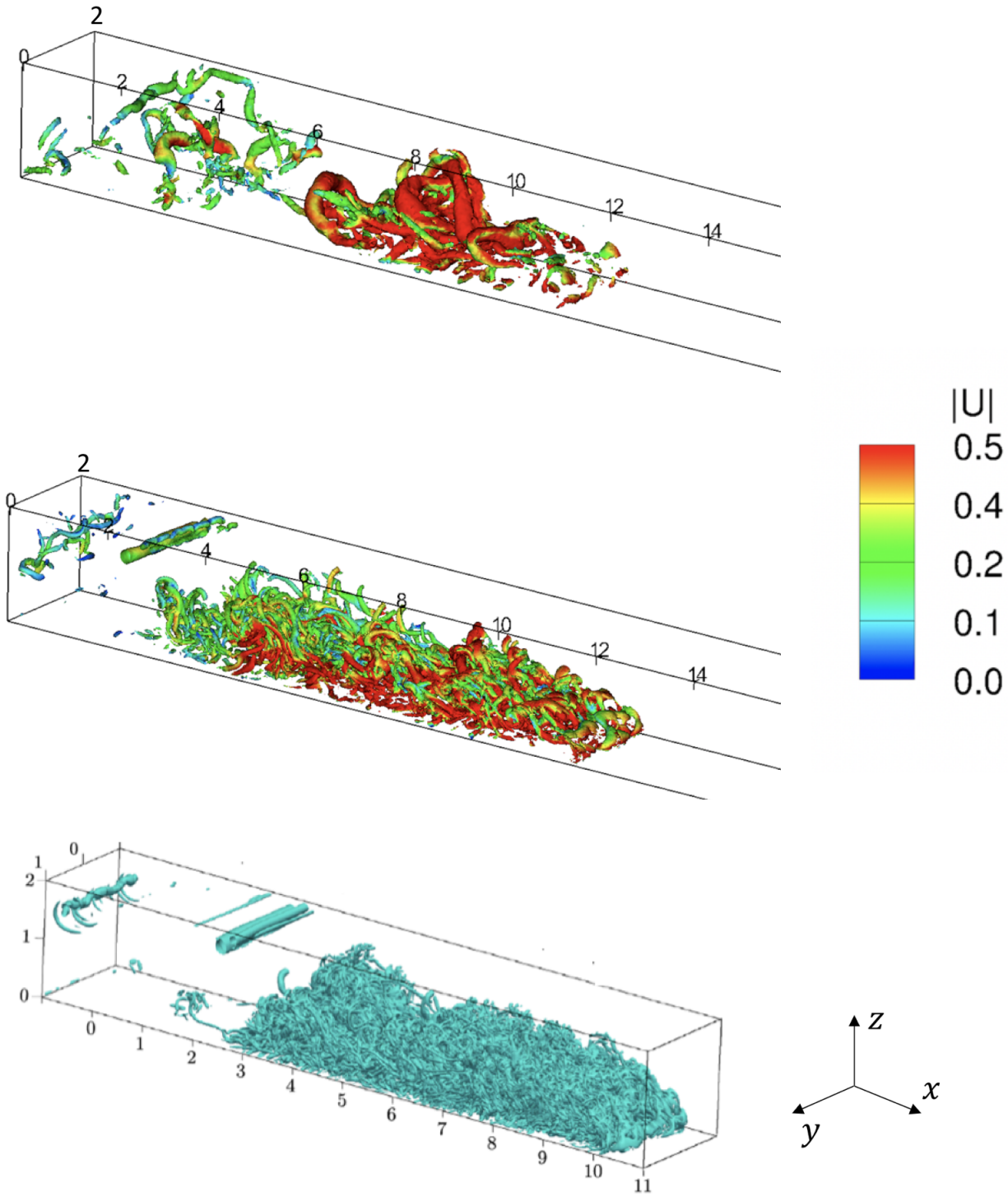

Figure 4.10: Vorticity structure by isosurfaces of Q-criterion (for the isovalue $Q = 1$) at $t = 20$. (coarse mesh, fine mesh, and DNS results from [59], from top to bottom)

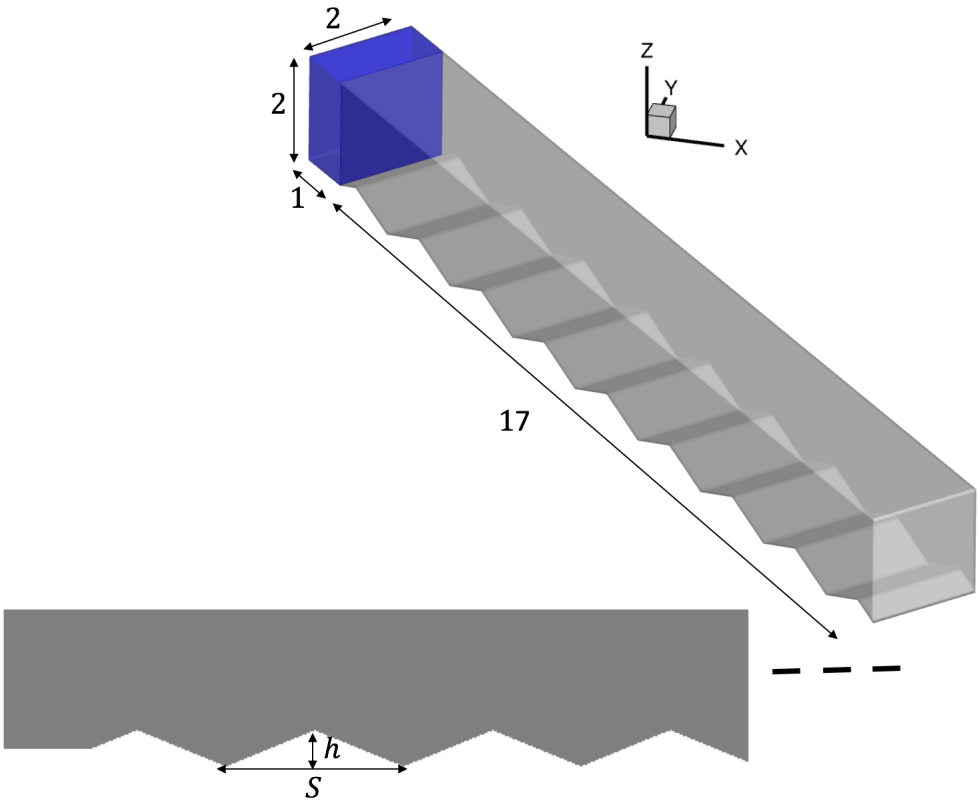

Figure 4.11: Computational setup of particle-laden gravity currents over triangular wavy terrains.

energy dissipation due to particle settling becomes higher.

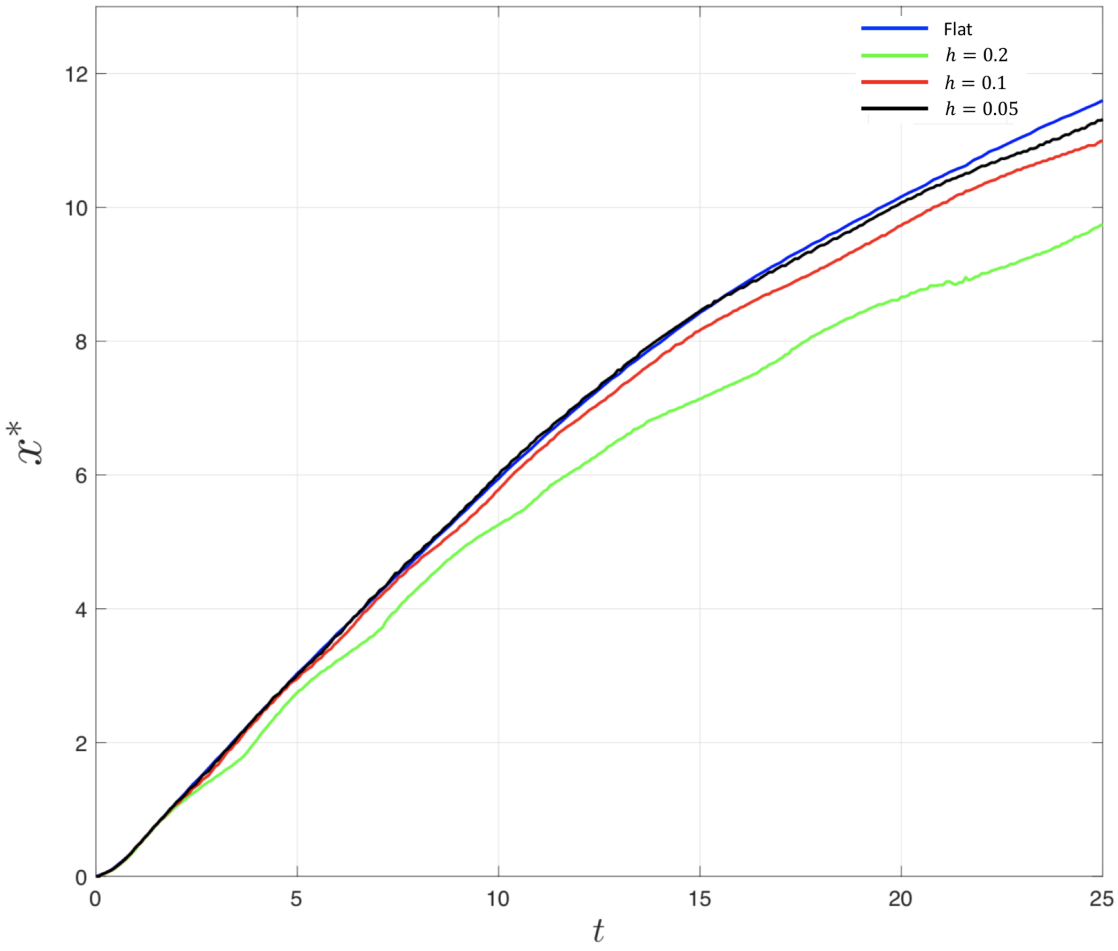

Figure 4.12: Time history of the front location of particle-laden gravity currents over triangular wavy terrains.

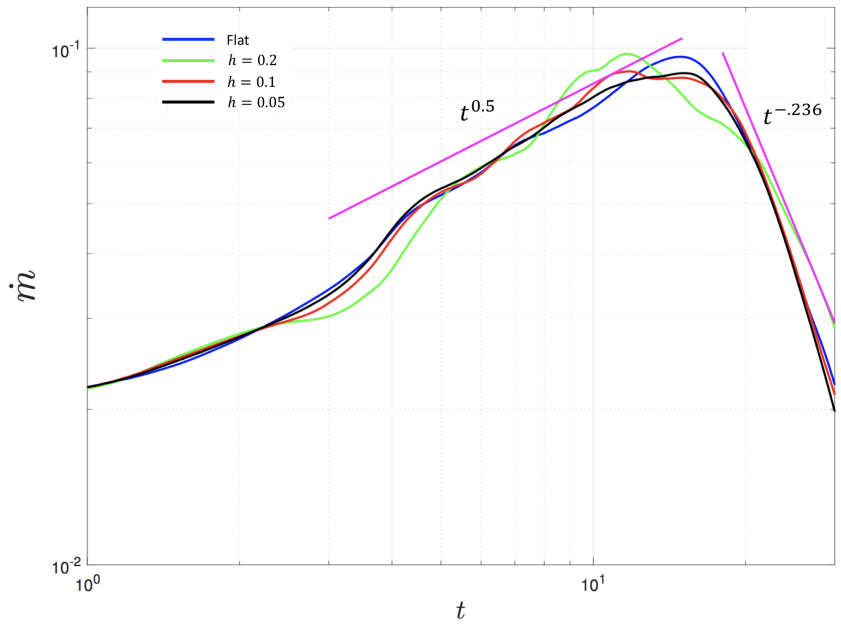

Figure 4.13: Time history of the sedimentation rate of particle-laden gravity currents over triangular wavy terrains.

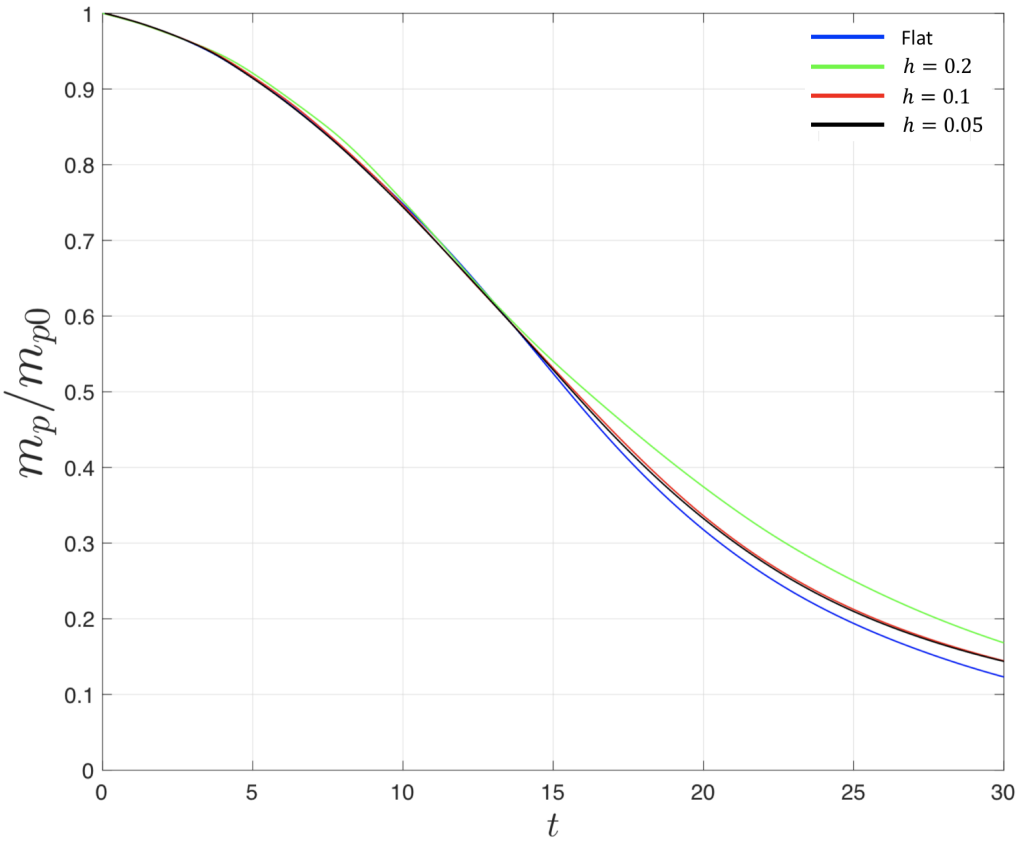

Figure 4.14: Time history of the normalized suspended mass of particle-laden gravity currents over triangular wavy terrains.

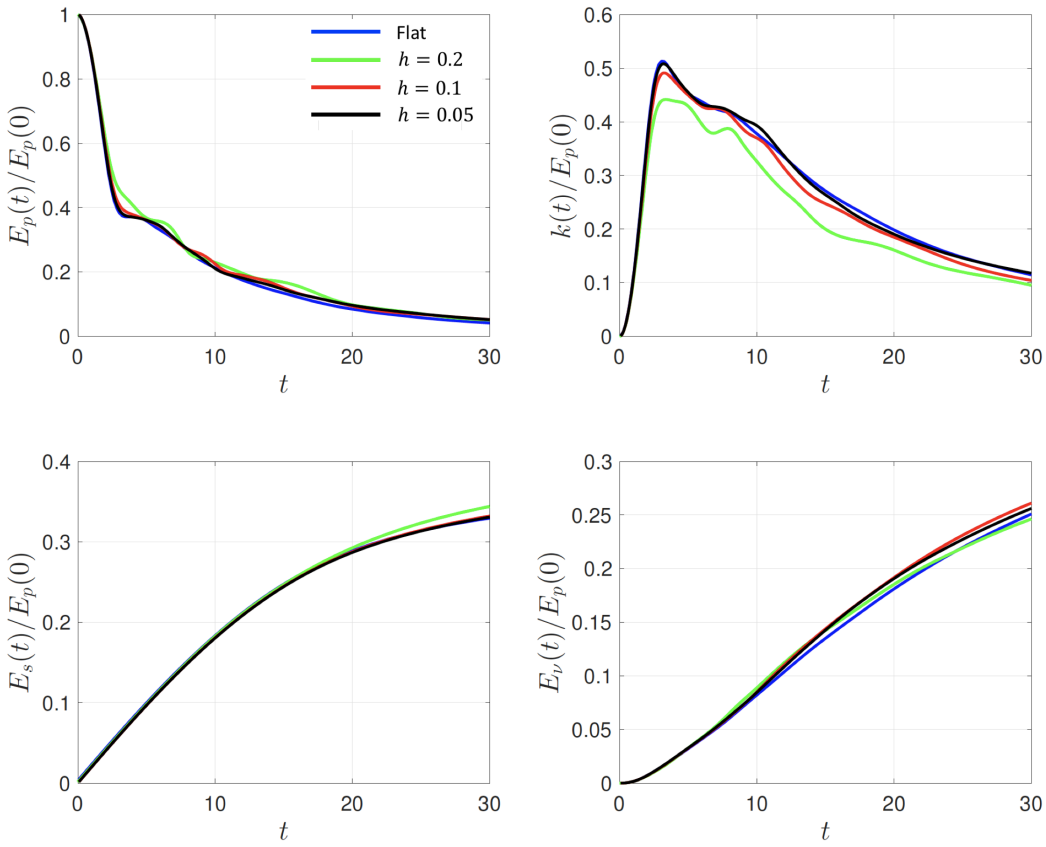

Figure 4.15: Time history of the kinetic energy $k(t)$, potential energy $E_p(t)$, the energy dissipation $E_v(t)$, and $E_s(t)$ normalized by the initial potential energy $E_p(0)$.

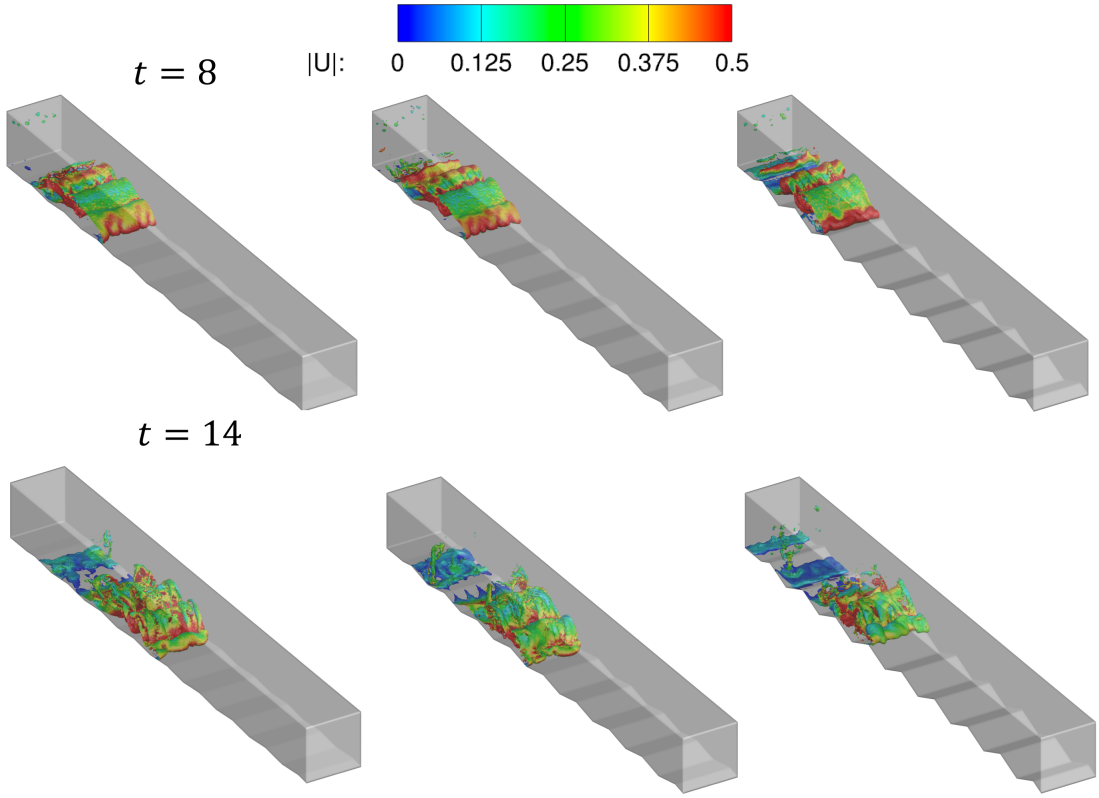

Figure 4.16: Interface evolution of $\rho = 0.25$ of particle-laden gravity currents over triangular wavy terrains. ($h = 0.05$, 0.1 and 0.2, from left to right).

Chapter 5

Future Work and Conclusions

In this project, we build a framework of simulate particle-laden currents only simulate the simple configuration. In the future, more complex configuration of simulation are willing to design. For example, different the shape of terrain and texture of surface.

A new numerical formulation for particle-laden gravity currents is presented using the framework of RBVMS methods. Inspired by the ideas from stabilized methods for convective–diffusive systems and compressible flows, a new set of the fine-scales parameters that introduces coupling between the fine-scale velocity and density-equation residual is proposed. The simulation of lock-exchange particle-laden gravity currents over flat terrain is performed using the proposed formulation. The computed results are validated by high-resolution computational results and experimental results reported by other researchers. The proposed formulation is proved to be able to reproduce highly accurately results without using high mesh resolution. Then the simulations of lock-exchange particle-laden gravity currents over triangular wavy terrains with different wave height are performed. We found the flow behavior is changed significantly, as the wave height increases. Increasing the wave height will decrease the current front speed, slow down the particle settling, prohibit the conversion of potential energy into kinetic energy.

References

[1] John E Simpson. *Gravity currents: In the environment and the laboratory*. Cambridge university press, 1997.

[2] T Brooke Benjamin. Gravity currents and related phenomena. *Journal of Fluid Mechanics*, 31(2):209–248, 1968.

[3] Eckart Meiburg, Senthil Radhakrishnan, and Mohamad Nasr-Azadani. Modeling gravity and turbidity currents: computational approaches and challenges. *Applied Mechanics Reviews*, 67(4):040802, 2015.

[4] Eckart Meiburg and Ben Kneller. Turbidity currents and their deposits. *Annual Review of Fluid Mechanics*, 42: 135–156, 2010.

[5] T Maxworthy, JSJE Leilich, JE Simpson, and EH Meiburg. The propagation of a gravity current into a linearly stratified fluid. *Journal of Fluid Mechanics*, 453:371–394, 2002.

[6] Herbert E Huppert. Gravity currents: a personal perspective. *Journal of Fluid Mechanics*, 554:299–322, 2006.

[7] NA Konopliv, Stefan G Llewellyn Smith, JN McElwaine, and E Meiburg. Modelling gravity currents without an energy closure. *Journal of Fluid Mechanics*, 789:806–829, 2016.

[8] James W Rottman and John E Simpson. Gravity currents produced by instantaneous releases of a heavy fluid in a rectangular channel. *Journal of Fluid Mechanics*, 135:95–110, 1983.

[9] Charlotte Gladstone and Andrew W Woods. On the application of box models to particle-driven gravity currents. *Journal of fluid mechanics*, 416:187–195, 2000.

[10] MM Nasr-Azadani and E Meiburg. Turbidity currents interacting with three-dimensional seafloor topography. *Journal of Fluid Mechanics*, 745:409–443, 2014.

[11] Carlos Härtel, Fredrik Carlsson, and Mattias Thunblom. Analysis and direct numerical simulation of the flow at a gravity-current head. part 2. the lobe-and-cleft instability. *Journal of Fluid Mechanics*, 418:213–229, 2000.

[12] Carlos Härtel, Eckart Meiburg, and Frieder Necker. Analysis and direct numerical simulation of the flow at a gravity-current head. part 1. flow topology and front speed for slip and no-slip boundaries. *Journal of Fluid Mechanics*, 418:189–212, 2000.

[13] Frieder Necker, Carlos Härtel, Leonhard Kleiser, and Eckart Meiburg. Mixing and dissipation in particle-driven gravity currents. *Journal of Fluid Mechanics*, 545:339–372, 2005.

[14] E Gonzalez-Juez, E Meiburg, T Tokyay, and G Constantinescu. Gravity current flow past a circular cylinder: forces, wall shear stresses and implications for scour. *Journal of Fluid Mechanics*, 649:69–102, 2010.

[15] Talia Tokyay, George Constantinescu, and Eckart Meiburg. Lock-exchange gravity currents with a high volume of release propagating over a periodic array of obstacles. *Journal of Fluid Mechanics*, 672:570–605, 2011.

[16] Mariano I Cantero, JR Lee, S Balachandar, and Marcelo H Garcia. On the front velocity of gravity currents. *Journal of Fluid Mechanics*, 586:1–39, 2007.

[17] BM Marino, LP Thomas, and PF Linden. The front condition for gravity currents. *Journal of Fluid Mechanics*, 536:49–78, 2005.

[18] Francois Blanchette, Martin Strauss, Eckart Meiburg, Benjamin Kneller, and Michael E Glinsky. High-resolution numerical simulations of resuspending gravity currents: Conditions for self-sustainment. *Journal of Geophysical Research: Oceans*, 110(C12), 2005.

[19] Frieder Necker, C Härtel, L Kleiser, and E Meiburg. High-resolution simulations of particle-driven gravity currents. *International Journal of Multiphase Flow*, 28(2):279–300, 2002.

[20] Renato N Elias, Paulo LB Paraizo, and Alvaro LGA Coutinho. Stabilized edge-based finite element computation of gravity currents in lock-exchange configurations. *International Journal for Numerical Methods in Fluids*, 57 (9):1137–1152, 2008.

[21] Gabriel M Guerra, Souleymane Zio, Jose J Camata, Fernando A Rochinha, Renato N Elias, Paulo LB Paraizo, and Alvaro LGA Coutinho. Numerical simulation of particle-laden flows by the residual-based variational multiscale method. *International Journal for Numerical Methods in Fluids*, 73(8):729–749, 2013.

[22] J O'Callaghan, G Rickard, S Popinet, and C Stevens. Response of buoyant plumes to transient discharges investigated using an adaptive solver. *Journal of Geophysical Research: Oceans*, 115(C11), 2010.

[23] HR Hiester, MD Piggott, and PA Allison. The impact of mesh adaptivity on the gravity current front speed in a two-dimensional lock-exchange. *Ocean Modelling*, 38(1):1–21, 2011.

[24] S Koltakov and OB Fringer. Moving grid method for numerical simulation of stratified flows. *International Journal for Numerical Methods in Fluids*, 71(12):1524–1545, 2013.

[25] Andre L Rossa and Alvaro LGA Coutinho. Parallel adaptive simulation of gravity currents on the lock-exchange problem. *Computers & Fluids*, 88:782–794, 2013.

[26] Y. Bazilevs, V. M. Calo, J. A. Cottrell, T. J. R. Hughes, A. Reali, and G. Scovazzi. Variational multiscale residual-based turbulence modeling for large eddy simulation of incompressible flows. *Computer Methods in Applied Mechanics and Engineering*, 197:173–201, 2007.

[27] K. Takizawa, Y. Bazilevs, T. E. Tezduyar, Ming-Chen Hsu, O. Øiseth, K. M. Mathisen, N. Kostov, and S. McIntyre. Engineering analysis and design with ALE-VMS and space–time methods. *Archives of Computational Methods in Engineering*, 21:481–508, 2014. doi: 10.1007/s11831-014-9113-0.

[28] Kenji Takizawa, Yuri Bazilevs, Tayfun E Tezduyar, Christopher C Long, Alison L Marsden, and Kathleen Schjodt. St and ale-vms methods for patient-specific cardiovascular fluid mechanics modeling. *Mathematical Models and Methods in Applied Sciences*, 24(12):2437–2486, 2014.

[29] Yuri Bazilevs, Ming-Chen Hsu, Kenji Takizawa, and Tayfun E Tezduyar. Ale-vms and st-vms methods for computer modeling of wind-turbine rotor aerodynamics and fluid–structure interaction. *Mathematical Models and Methods in Applied Sciences*, 22(supp02):1230002, 2012.

[30] Y. Bazilevs and I. Akkerman. Large eddy simulation of turbulent Taylor–Couette flow using isogeometric analysis and the residual–based variational multiscale method. *Journal of Computational Physics*, 229:3402–3414, 2010.

[31] Y Bazilevs, J Yan, M de Stadler, and S Sarkar. Computation of the flow over a sphere at re= 3700: A comparison of uniform and turbulent inflow conditions. *Journal of Applied Mechanics*, 81(12):121003, 2014.

[32] Roozbeh Golshan, Andrés E Tejada-Martínez, Mario Juha, and Yuri Bazilevs. Large-eddy simulation with near-wall modeling using weakly enforced no-slip boundary conditions. *Computers & Fluids*, 118:172–181, 2015.

[33] AndrÃŠs E Tejada-MartÃnez, Ido Akkerman, and Yuri Bazilevs. Large-eddy simulation of shallow water langmuir turbulence using isogeometric analysis and the residual-based variational multiscale method. *Journal of Applied Mechanics*, 79(1):010909, 2012.

[34] Fei Xu, Dominik Schillinger, David Kamensky, Vasco Varduhn, Chenglong Wang, and Ming-Chen Hsu. The tetrahedral finite cell method for fluids: Immersogeometric analysis of turbulent flow around complex geometries. *Computers & Fluids*, 2015.

[35] Timo M van Opstal, Jinhui Yan, Chris Coley, John A Evans, Trond Kvamsdal, and Yuri Bazilevs. Isogeometric divergence-conforming variational multiscale formulation of incompressible turbulent flows. *Computer Methods in Applied Mechanics and Engineering*, 2016.

[36] J Yan, A Korobenko, AE Tejada-Martínez, R Golshan, and Y Bazilevs. A new variational multiscale formulation for stratified incompressible turbulent flows. *Computers & Fluids*, 2016.

[37] Y Bazilevs, K Kamran, G Moutsanidis, DJ Benson, and E Oñate. A new formulation for air-blast fluid–structure interaction using an immersed approach. part i: basic methodology and fem-based simulations. *Computational Mechanics*, pages 1–18, 2017.

[38] Y Bazilevs, G Moutsanidis, J Bueno, K Kamran, D Kamensky, MC Hillman, H Gomez, and JS Chen. A new formulation for air-blast fluid–structure interaction using an immersed approach: part iicoupling of iga and meshfree discretizations. *Computational Mechanics*, pages 1–16, 2017.

[39] T. E. Tezduyar. Stabilization parameters and element length scales in SUPG and PSPG formulations. In *Book of Abstracts of An Euro Conference on Numerical Methods and Computational Mechanics*, Miskolc, Hungary, 2002.

[40] T. E. Tezduyar. Computation of moving boundaries and interfaces with interface-tracking and interface-capturing techniques. In *Pre-Conference Proceedings of the Sixth Japan-US International Symposium on Flow Simulation and Modeling*, Fukuoka, Japan, 2002.

[41] T. E. Tezduyar. Finite element methods for fluid dynamics with moving boundaries and interfaces. In E. Stein, R. De Borst, and T. J. R. Hughes, editors, *Encyclopedia of Computational Mechanics*, Volume 3: Fluids, chapter 17. John Wiley & Sons, 2004.

[42] T. E. Tezduyar. Finite elements in fluids: Stabilized formulations and moving boundaries and interfaces. *Computers & Fluids*, 36:191–206, 2007. doi: 10.1016/j.compfluid.2005.02.011.

[43] T. E. Tezduyar and T. J. R. Hughes. Finite element formulations for convection dominated flows with particular emphasis on the compressible Euler equations. In *Proceedings of AIAA 21st Aerospace Sciences Meeting*, AIAA Paper 83-0125, Reno, Nevada, 1983.

[44] T. J. R. Hughes, W. K. Liu, and T. K. Zimmermann. Lagrangian–Eulerian finite element formulation for incompressible viscous flows. *Computer Methods in Applied Mechanics and Engineering*, 29:329–349, 1981.

[45] J Yan, A Korobenko, X Deng, and Y Bazilevs. Computational free-surface fluid–structure interaction with application to floating offshore wind turbines. *Computers & Fluids*, 2016.

[46] J Yan, X Deng, A Korobenko, and Y Bazilevs. Free-surface flow modeling and simulation of horizontal-axis tidal-stream turbines. *Computers & Fluids*, 2016.

[47] Y Bazilevs, A Korobenko, X Deng, and J Yan. Fluid–structure interaction modeling for fatigue-damage prediction in full-scale wind-turbine blades. *Journal of Applied Mechanics*, 83(6):061010, 2016.

[48] B. Augier, J. Yan, A. Korobenko, J. Czarnowski, G. Ketterman, and Y. Bazilevs. Experimental and numerical FSI study of compliant hydrofoils. 2014. Published online. DOI:10.1007/s00466-014-1090-5.

[49] J Yan, B Augier, A Korobenko, J Czarnowski, G Ketterman, and Y Bazilevs. Fsi modeling of a propulsion system based on compliant hydrofoils in a tandem configuration. *Computers & Fluids*, 2015.

[50] K. Takizawa, Y. Bazilevs, and T. E. Tezduyar. Space–time and ALE-VMS techniques for patient-specific cardiovascular fluid–structure interaction modeling. *Archives of Computational Methods in Engineering*, 19:171–225, 2012. doi: 10.1007/s11831-012-9071-3.

[51] K. Takizawa, Y. Bazilevs, T. E. Tezduyar, C. C. Long, A. L. Marsden, and K. Schjodt. ST and ALE-VMS methods for patient-specific cardiovascular fluid mechanics modeling. *Mathematical Models and Methods in Applied Sciences*, 24:2437–2486, 2014.

[52] Kenji Takizawa, Yuri Bazilevs, and Tayfun E Tezduyar. Space–Time and ALE-VMS techniques for patient-specific cardiovascular fluid–structure interaction modeling. *Archives of Computational Methods in Engineering*, 19(2):171–225, 2012.

[53] Kenji Takizawa, Tayfun E Tezduyar, and Takashi Kuraishi. Multiscale space–time methods for thermo-fluid analysis of a ground vehicle and its tires. *Mathematical Models and Methods in Applied Sciences*, 25(12): 2227–2255, 2015.

[54] Fei Xu, George Moutsanidis, David Kamensky, Ming-Chen Hsu, Muthuvel Murugan, Anindya Ghoshal, and Yuri Bazilevs. Compressible flows on moving domains: Stabilized methods, weakly enforced essential boundary conditions, sliding interfaces, and application to gas-turbine modeling. *Computers & Fluids*, 158:201–220, 2017.

[55] Tore A Helgedagsrud, Yuri Bazilevs, Artem Korobenko, Kjell M Mathisen, and Ole A Øiseth. Using ale-vms to compute aerodynamic derivatives of bridge sections. *Computers & Fluids*, 2018.

[56] M.-C. Hsu, D. Kamensky, Y. Bazilevs, M. S. Sacks, and T. J. R. Hughes. Fluid–structure interaction analysis of bioprosthetic heart valves: significance of arterial wall deformation. 54:1055–1071, 2014. doi: 10.1007/s00466-014-1059-4.

[57] D. Kamensky, M.-C. Hsu, D. Schillinger, J.A. Evans, A. Aggarwal, Y. Bazilevs, M.S. Sacks, and T.JR. Hughes. An immersogeometric variational framework for fluid–structure interaction: Application to bioprosthetic heart valves. 284:1005–1053, 2015.

[58] George Constantinescu. Les of lock-exchange compositional gravity currents: a brief review of some recent results. *Environmental Fluid Mechanics*, 14(2):295–317, 2014.

[59] LFR Espath, LC Pinto, S Laizet, and JH Silvestrini. Two-and three-dimensional direct numerical simulation of particle-laden gravity currents. *Computers & Geosciences*, 63:9–16, 2014.

[60] F. Shakib, T. J. R. Hughes, and Z. Johan. A multi-element group preconditionined GMRES algorithm for non-symmetric systems arising in finite element analysis. *Computer Methods in Applied Mechanics and Engineering*, 75:415–456, 1989.

[61] T. J. R. Hughes and M. Mallet. A new finite element formulation for computational fluid dynamics: III. The generalized streamline operator for multidimensional advective-diffusive systems. *Computer Methods in Applied Mechanics and Engineering*, 58:305–328, 1986.

[62] T. J. R. Hughes, G. Scovazzi, and T. E. Tezduyar. Stabilized methods for compressible flows. *Journal of Scientific Computing*, 43:343–368, 2010. doi: 10.1007/s10915-008-9233-5. DOI: 10.1007/s10915-008-9233-5.

[63] Isaac Harari and Thomas JR Hughes. What are c and h?: Inequalities for the analysis and design of finite element methods. *Computer Methods in Applied Mechanics and Engineering*, 97(2):157–192, 1992.

[64] A. N. Brooks and T. J. R. Hughes. Streamline upwind/Petrov-Galerkin formulations for convection dominated flows with particular emphasis on the incompressible Navier-Stokes equations. *Computer Methods in Applied Mechanics and Engineering*, 32:199–259, 1982.

[65] Ming-Chen Hsu, Y. Bazilevs, V. M. Calo, T. E. Tezduyar, and T. J. R. Hughes. Improving stability of stabilized and multiscale formulations in flow simulations at small time steps. *Computer Methods in Applied Mechanics and Engineering*, 199:828–840, 2010. doi: 10.1016/j.cma.2009.06.019.

[66] K. Takizawa, S. Sathe, and T. E. Tezduyar. Incompressible flow computations with the multi-moment and SUPG/PSPG formulations. In *Proceedings of the Third Asian-Pacific Congress on Computational Mechanics (CD-ROM)*, Kyoto, Japan, 2007.

[67] T. Tezduyar and S. Sathe. Stabilization parameters in SUPG and PSPG formulations. *Journal of Computational and Applied Mechanics*, 4:71–88, 2003.

[68] T. E. Tezduyar, J. Liou, D. K. Ganjoo, M. Behr, and R. Glowinski. Unsteady incompressible flow computations with the finite element method. In T. J. Chung, editor, *Finite Elements in Fluids*, Vol.8, pages 177–209. Hemisphere Publishing, 1992.

[69] T. E. Tezduyar, S. Mittal, S. E. Ray, and R. Shih. Incompressible flow computations with stabilized bilinear and linear equal-order-interpolation velocity-pressure elements. *Computer Methods in Applied Mechanics and Engineering*, 95:221–242, 1992. doi: 10.1016/0045-7825(92)90141-6.

[70] F De Rooij and S Dalziel. Time-and space-resolved measurements of deposition under turbidity currents. *Particulate Gravity Currents, Wiley, New York*, pages 207–215, 2009.